Asian Journal of Chemistry; Vol. 37, No. 12 (2025), 3183-3190
ASIAN JOURNAL OF CHEMISTRY
https://doi.org/10.14233/ajchem.2025.34789

Thermo-Electrical Performance of Ferrite-Doped Chitosan Nanocomposites Modified with Graphene Oxide

SANJEETA RANI[1], PRITI GOYAL[1], LAISHRAM SAYA[2], SUNITA HOODA[3] and MANISHA VERMA[1,*]

[1]Department of Physics, Acharya Narendra Dev College, University of Delhi, Govindpuri, Kalkaji, New Delhi-110019, India
[2]Department of Chemistry, Sri Venkateswara College, University of Delhi, Dhaula Kuan, New Delhi-110021, India
[3]Polymer Research Laboratory, Department of Chemistry, Acharya Narendra Dev College, University of Delhi, Govindpuri, Kalkaji, New Delhi-110019, India

*Corresponding author: E-mail: manishaverma@andc.du.ac.in

Received: 26 July 2025 *Accepted*: 24 November 2025 *Published online*: 30 November 2025 AJC-22210

The growing demand for renewable, multifunctional materials has spurred interest in nanocomposites for energy, biomedical and environmental uses. In this study, magnetic chitosan (MCS) and magnetic chitosan–graphene oxide (MCS/GO) nanocomposites were synthesized *via* a simple coprecipitation method. The structural, thermal and electrochemical properties were analyzed using XRD, FESEM-EDAX, TGA and impedance spectroscopy. XRD confirmed nanocrystalline phases (7.6 nm) with uniform magnetite dispersion in the polymer–GO matrix. TGA showed a residual mass of ~88% at 800 ºC for MCS/GO, indicating high thermal stability. Impedance analysis showed easier charge movement through the bulk at higher frequencies; both resistance and reactance decreased with temperature, confirming thermally activated transport. The activation energy (~168 meV) indicates efficient GO-assisted carrier hopping, making MCS/GO nanocomposites promising for energy-efficient sensors, solid-state batteries and thermally stable electronic devices.

Keywords: Magnetic chitosan, Graphene oxide, Nanocomposite, Thermal stability, Impedance spectroscopy.

INTRODUCTION

The growing demand for sustainable and multifunctional materials has catalyzed significant interest in bio-based nanocomposites. Among them, chitosan, a natural polysaccharide derived from the deacetylation of chitin, stands out due to its biodegradability, biocompatibility and rich chemical functionality. All these attributes make chitosan apt for many applications like biomedicine, electronic devices and water purification [1,2].

To improve the performance and applications of chitosan, magnetic nanoparticles especially magnetite (Fe_3O_4), are often incorporated into its structure, creating magnetic chitosan (MCS). Such a material exhibits superparamagnetic behaviour as well as superior mechanical strength in contrast to pure chitosan. The incorporation of magnetic nanoparticles also introduces additional active sites and increases the overall surface area, which enables better interaction with surrounding molecules. This also improves the nanocomposites' chelation capacity and reactivity thereby establishing direct connection between enhanced properties and processing techniques [3,4]. These features make MCS a viable and attractive material to be used in diverse fields like biosensing, drug administration and environmental remediation [5]. Nevertheless, challenges such as limited electrical conductivity and structural instability under specific environmental conditions hinder its application in advanced biomedical and electronic technologies.

Graphene oxide (GO), a chemically modified derivative of graphene, has emerged as a promising additive for polymer matrices due to its exceptional mechanical strength, thermal stability, electrical conductivity and abundance of oxygenated functional groups like hydroxyl, carboxyl and epoxide [6,7]. Incorporating GO into chitosan matrices improves their biocompatibility, adsorption efficiency and structural integrity [1].

When graphene oxide (GO) is combined with magnetic chitosan, the resulting nanocomposite shows noticeable improvement in its thermal as well as mechanical properties. The presence of GO also improves electrical conductivity, making the material even more versatile for advanced technological applications. These magnetic chitosan–graphene oxide (MCS/GO) composites are thus positioned as promising candidates

for use in electrochemical sensors, flexible electronics, energy storage devices and biomedical systems [8].

The dielectric and impedance characteristics of magnetic polymer composites have been the subject of increasing attention. Studies on Fe_3O_4-doped chitosan have revealed frequency-dependent electrical conductivity and dielectric relaxation phenomena, reinforcing the material's relevance to electronic applications [9]. Likewise, functionalized biopolymers, such as EDTA-modified chitin, have exhibited tailored thermal and dielectric behaviours that are favourable for niche technological uses [10]. Furthermore, integrating GO into polymer networks has consistently shown to boost both mechanical resilience and electrical performance, thereby expanding the range of nanocomposite applications [11]. However, there is a practical limitation in the usage of MCS material alone as it has low conductivity and mechanical durability. The inclusion of GO within the MCS framework is expected to overcome these drawbacks by providing enhanced structural reinforcement and improved electrochemical characteristics [12].

Given the combination of magnetic responsiveness, dielectric tunability and mechanical robustness, MCS and MCS/GO nanocomposites offer considerable potential in various high-performance domains, especially in biomedical engineering and electronics [13,14]. However, there are still few studies that relate dielectric behaviour, magnetic response and structural stability of MCS/GO materials together as a single system. The present study not only evaluates these properties independently but also explores the ways in which they influence one another. By analyzing results from XRD, TGA and impedance spectroscopy, we explain how GO influences the material's decomposition and charge transport properties. This combined analysis allows us to understand the relation between internal structure of the nanocomposite and its thermal stability and electrical behaviour. Results show GO's dual role as a stabilizing and charge-facilitating agent. This integrated approach connects the thermal stability, microstructure and carrier dynamics, offering useful insights for designing bio-derived materials for sustainable energy, environmental and biomedical applications.

EXPERIMENTAL

All chemicals employed in this study were of analytical grade, so no further purification was necessary. Ammonia solution (NH_3, 25 wt.%), ferric chloride ($FeCl_3$, 96.0%), ferrous chloride ($FeCl_2$, 96.0%) and chitosan (99%) were acquired from Merck Ltd., India. Sigma-Aldrich provided the graphite (99%), which require to prepare graphene oxide (GO). A modified enhanced Hummer's method was used to prepare GO, whilst a coprecipitation technique was used to prepare MCS and MCS/GO. During the entire synthesis procedure, double-distilled water was utilized.

Synthesis of graphene oxide (GO): Graphene oxide (GO) was synthesized using a modified Hummer's process [15]. After adding 1.0 g of graphite flakes to 25 mL of 98% H_2SO_4 in an RB flask and stirring magnetically for 2 h, 3 g of $KMnO_4$ was gradually added to keep the temperature below 5 ºC. The mixture was agitated for a further 2 h while the temperature was kept at 40 ºC in a water bath. Following the addition of further deionized water (about 50 mL), an exothermic reaction occurred, raising the mixture's temperature to above 90 ºC. A fine brownish-yellow solid was produced after 1 mL of 30% H_2O_2 was added to stop the oxidation. Finally, 37% HCl rinses were used alternately to repeatedly wash and filter the product.

Synthesis of magnetic chitosan (MCS): After 10 min of magnetic swirling, separate solutions of $FeCl_3$ (0.1 M, 25 mL) and $FeCl_2$ (0.05 M, 25 mL) were combined and swirled for 30 min at room temperature. When dropwise, 25 mL of diluted NaOH solution was added, the yellow solution that had been produced by the addition of chitosan (CS) transformed into a black precipitate. The resulted solid MCS was then washed and vacuum-dried for 24 h at 40 ºC, producing a dark brown powder.

Synthesis of MCS/GO: The MCS/GO nanocomposite was prepared using a simple coprecipitation method [16], which involves doping graphene oxide (GO) onto magnetized chitosan (MCS). To start the process, 25 mL of aqueous solutions of $FeCl_3$ and $FeCl_2$ in a 2:1 molar ratio was prepared. A GO dispersion (2 mg in 10 mL of deionized water) and a chitosan solution (2 mg in 50 mL of deionized water) were sonicated separately for 1 h. After that, these two solutions were combined and agitated for one more hour. The separation of black solid (MCS/GO), which was created by the coprecipitation of magnetite nanoparticles with the nanocomposite, was achieved in the last step by adding 3 mL of diluted NaOH dropwise.

Characterization: Several physico-analytical methods were used to characterize the as-synthesized material. A Bruker D8 Discover diffractometer was used to record X-ray diffraction (XRD) spectra. Thermogravimetric scans were recorded using a TGA HiRes 1000 thermal analyzer by heating the powder samples in an alumina pan at 10 ºC/min under a nitrogen flow of 20 mL/min. FESEM images were captured using a Zeiss Gemini SEM 500 thermal field emission system. The samples were pelletized and coated with silver paste for impedance analysis. Measurements were carried out under a bias voltage of 1 V DC throughout a broad frequency range of 1 Hz to 10 MHz and a temperature range of 293 K to 373 K using a dielectric/impedance analyzer (Novocontrol Technologies, Germany) equipped with an automatic data acquisition and display system. The experimental data was analyzed and plotted using OriginPro and Python.

RESULTS AND DISCUSSION

XRD studies: The crystalline structure of the MCS/GO nanocomposite was analyzed using X-ray diffraction over a 2θ range of 10-60º. The resulting pattern (Fig. 1) shows distinct diffraction peaks characteristic of the inverse spinel structure of Fe_3O_4 (magnetite), in accordance with the standard JCPDS card No. 19-0629 [17]. Among these the most intense reflection is observed at $2\theta \approx 35.5º$, which corresponds to the (311) plane and is considered to be the fingerprint of magnetite. This peak confirms the presence of strongly crystalline Fe_3O_4 nanoparticles interspersed within the CS/GO matrix. It is important to note that peaks corresponding to secondary phases such as hematite (α-Fe_2O_3) or maghemite (γ-Fe_2O_3) are absent

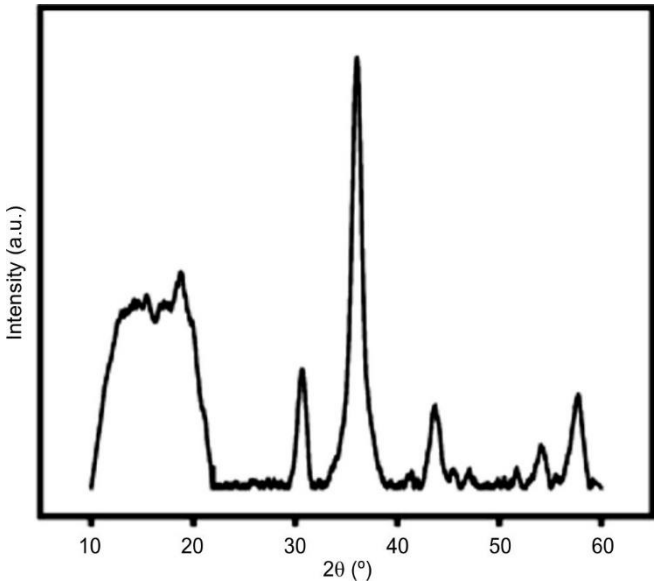

Fig. 1. XRD of MCS/GO nanocomposite

indicating purity of the ferrite phase. The breadth of the diffraction peaks reflects the nanoscale dimensions and internal strain of the crystallites. The Scherrer's equation, which reads $D = K\lambda/\beta\cos\theta$, was used to estimate the average crystallite size, where λ is the X-ray wavelength (1.5406 Å for Cu*K*α); β is the full width at half maximum (FWHM in radians), θ is the Bragg's angle; and D is the crystallite size. K is the shape factor (0.9). From the analysis of the dominant (311) peak, the crystallite size was calculated to be in the nanometer range (~7.6 nm), confirming the formation of nanostructured magnetite. For the (311) reflection at $2\theta \approx 35.5^{o}$, the lattice parameter was found to be ~ -8.4 Å, in close agreement with bulk Fe_3O_4 (8.396 Å). Small deviations from the standard value may arise from nanocrystalline effects, interfacial strain with GO/CS and possible oxygen vacancies within the spinel lattice.

The broad hump observed in the region 12-22º corresponds to the amorphous halo of chitosan and the disordered domains of graphene oxide [18]. The presence of chitosan, GO and Fe_3O_4 peaks in the XRD spectrum confirms the composite nature of the synthesized sample wherein crystalline Fe_3O_4 nanoparticles are uniformly dispersed in the GO matrix. Overall, the XRD examination validates that a phase-pure magnetite nanostructure was successfully synthesized, with crystallite sizes in the nanometer regime, well integrated into the CS/GO framework. The pronounced (311) peak highlights the stable and well-defined spinel structure of the ferrite phase, which plays a crucial role in understanding the composite's dielectric and electrochemical performance.

FESEM and EDAX studies: The SEM images of the magnetic chitosan/graphene oxide (MCS/GO) nanocomposite provide insights into its surface morphology and the degree of integration between the constituent components. Fig. 2a-b shows the MCS/GO FESEM images. The layered structure of GO is nearly destroyed in the images of MCS/GO and magnetic chitosan nanoparticles serve to adorn the layers of the GO network. Good dispersion and efficient interfacial contact are suggested by the rather homogeneous particle distribution on the GO sheets. The development of a functional nanocomposite appropriate for use in drug administration, magnetic separation or environmental cleanup is highly supported by this morphological data. The cumulative sum spectra, as shown in Fig. 2c, derived from EDAX analysis, display the chemical composition in terms of the percentage masses of C, N, O and Fe.

Thermal studies: The TGA analysis of MCS/GO shown in Fig. 3 also demonstrated a multistep decomposition process from room temperature to 800 ºC, similar to MCS [19]. The TGA curve (black line) shows a small weight loss up to about 118 ºC, which can be attributed to the evaporation of physically adsorbed water and residual moisture. A significant weight loss is observed between 250 ºC and 400 ºC probably due to the thermal decomposition of the chitosan backbone consisting of functional groups and linkages. The DTG curve (red line) exhibits a prominent peak in this region, indicating the main degradation step. Beyond 400 ºC, the weight loss gradually continues, likely due to the degradation of residual carbonaceous materials and the partial decomposition of functional groups such as carboxyl, hydroxyl and epoxy groups on GO. Moreover, the residual mass of MCS/GO at 800 ºC was approximately 88%, which is significantly greater than that of pure MCS showing that adding GO has significantly improved the stability [19]. Higher thermal stability of MCS/GO can be attributed to the intermolecular crosslinking reaction. The thermal profile confirms the structural integrity of the prepared composite at moderately high temperatures, which is essential for potential applications in environmental and catalytic systems.

Complex impedance-dielectric spectroscopic analysis: Complex impedance spectroscopy (CIS) is a powerful analytical technique used to investigate the electrical response of materials over a wide frequency range. It provides insight into charge transport, polarization phenomena and interfacial processes occurring between the electrodes and the sample. By analysing these charge-transfer and relaxation mechanisms, CIS offers a deeper understanding of the material's overall electrical behaviour and its underlying physico-chemical interactions. The real part (Z′) indicates the resistance of the material, while the imaginary part (Z″), also known as reactance, which reveals its capacitive behaviour. The material's capacitive energy storage and dielectric loss characteristics is reflected in Z″, the imaginary component of impedance. The imaginary component of impedance (Z″) primarily represents the dielectric relaxation behaviour of the material, indicating the reorientation of internal dipoles under an applied alternating electric field.

Frequency-dependent Z′ behaviour of MCS/GO nanocomposite: Fig. 4 illustrates the variation of Z′ with frequency at different temperatures. For temperatures below 353 K, Z′ initially decreases sharply with increase in frequency up to 10^4 Hz, then shows a slight plateau until 10^5 Hz, after which it decreases again. This observed behaviour of Z′ with frequency can be explained by understanding the interplay between charge transport and various polarization mechanisms occurring within the material [20].

Initial rapid decrease (up to 10^4 Hz): At lower frequencies, charge carriers have sufficient time to respond to the

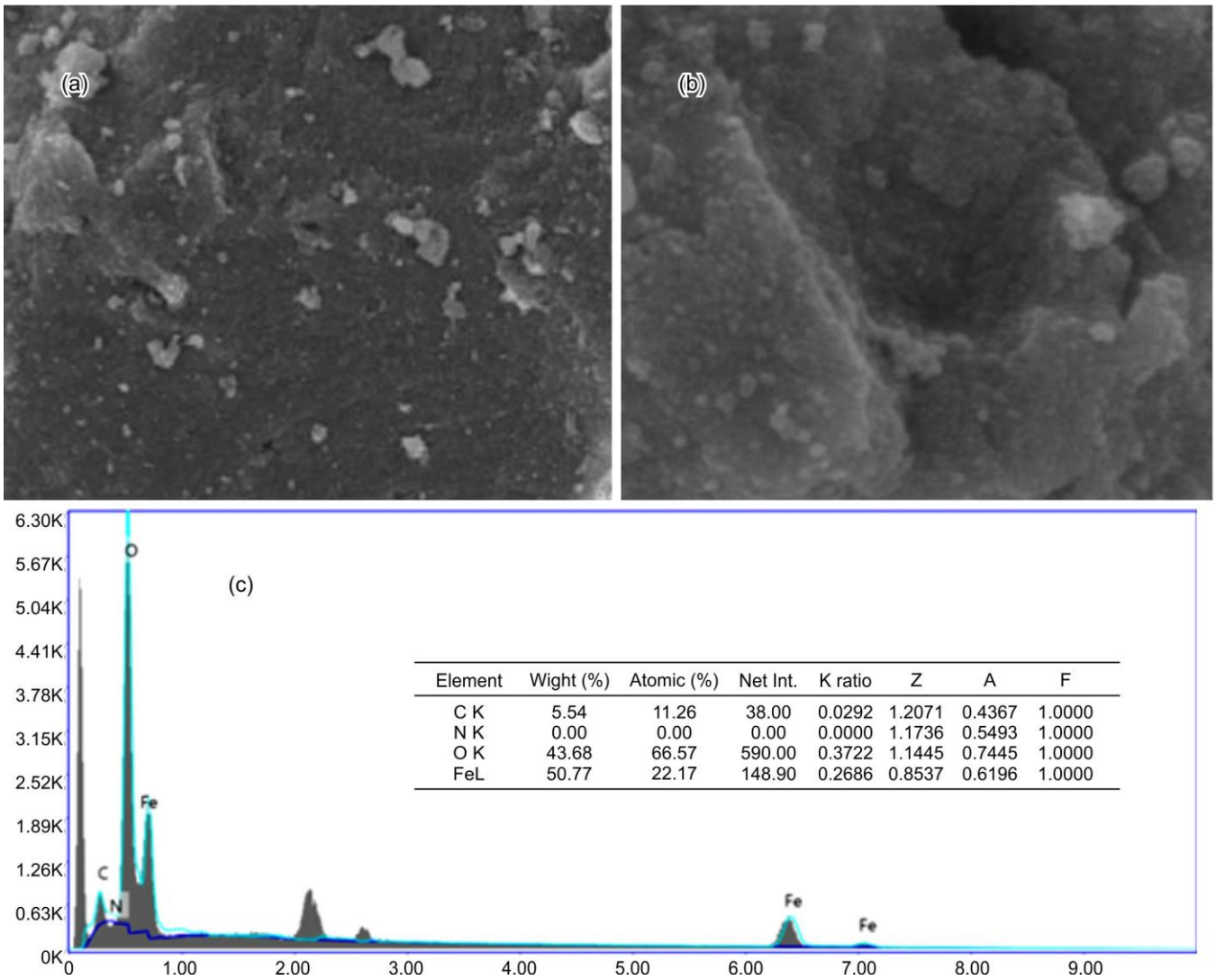

Element	Wight (%)	Atomic (%)	Net Int.	K ratio	Z	A	F
C K	5.54	11.26	38.00	0.0292	1.2071	0.4367	1.0000
N K	0.00	0.00	0.00	0.0000	1.1736	0.5493	1.0000
O K	43.68	66.57	590.00	0.3722	1.1445	0.7445	1.0000
FeL	50.77	22.17	148.90	0.2686	0.8537	0.6196	1.0000

Fig. 2. (a,b) FESEM images of MCS/GO, (c) Mass percentages compositions of the C, N, Fe and O

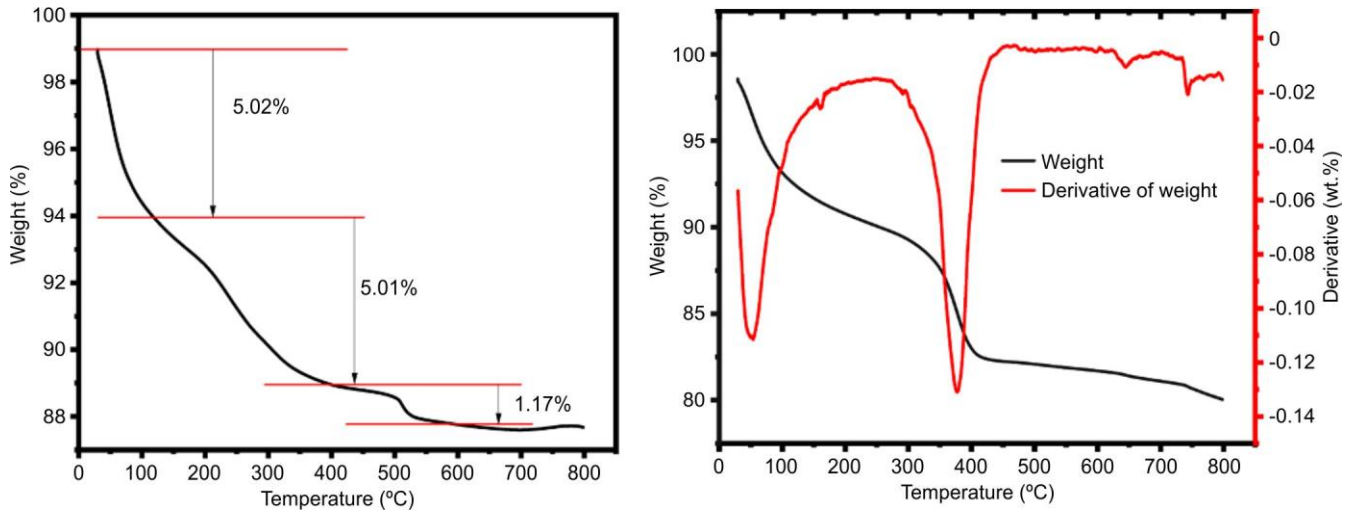

Fig. 3. TGA and DTG curves for MCS/GO

electric field, ensuing higher electrical conductivity and a reduction in Z′. This suggests the dominance of grain boundary resistance, which decreases as frequency increases.

(i) Slight decrease (between 10^4 and 10^5 Hz): In this lower-to-mid frequency range, interfacial and dipolar polarization effects play an important role in determining its beha-

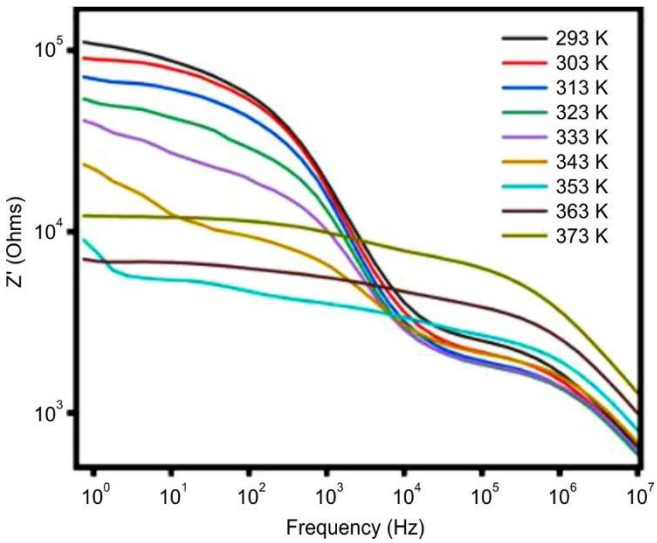

Fig. 4. Plot of Z′ *versus* frequency for MCS/GO at different temperatures

viour. Some charge carriers are not mobile enough to follow the rapidly alternating electric field, leading to localized charge buildup at interfaces. This restricted motion results in the observed increase in impedance, reflecting the material's difficulty in responding to faster field oscillations.

(ii) Final decrease (beyond 10^5 Hz): The polarization effects are not appreciable at frequencies causing a decrease in impedance. This is mainly attributed to increased charge carrier mobility and decreased resistance at grain boundaries [21]. Z′ further decreases as the system gets closer to the material's inherent bulk characteristics.

At low frequencies, this pattern shows a shift from grain boundary-dominated conduction to bulk-dominated conduction at high frequencies. It is also observed that this decrease becomes less pronounced for temperatures higher than 360 K.

Temperature-dependent Z′ behaviour of MCS/GO nanocomposite: Fig. 5 shows the temperature dependency of the real part of impedance (Z′) for the measurements made over a broad frequency range (2.73 Hz to 10 MHz). At all frequencies, Z′ exhibits a characteristic decreasing–increasing trend with rising temperature, resulting in a V-shaped profile. This behaviour highlights the relation between the nanocomposite's frequency-dependent relaxation processes and the temperature dependent charge carrier's movement. At low temperatures Z′ decreases as temperature increases, showing that conductivity improves when more charge carriers gain sufficient thermal energy to move. This effect is especially visible at low frequencies because in this region, interfacial polarization and space-charge effects dominate. The charges, at low frequencies, accumulate at the grain boundaries or interfaces, making the material appear more resistive. However, with increase in temperature charges become more mobile and move more freely, resulting in a further decrease in Z′ [22].

The minimum value of Z′ is observed around 350 K for frequencies upto 10^3 Hz. At temperatures higher than 350 K, Z′ again rises due to reduced charge mobility due to the structural rearrangements or increased phonon scattering. Moreover, further heating may also cause slight degradation of the chitosan matrix or rearrangement of the magnetic and GO domains which in turn affects charge transport increasing Z′.

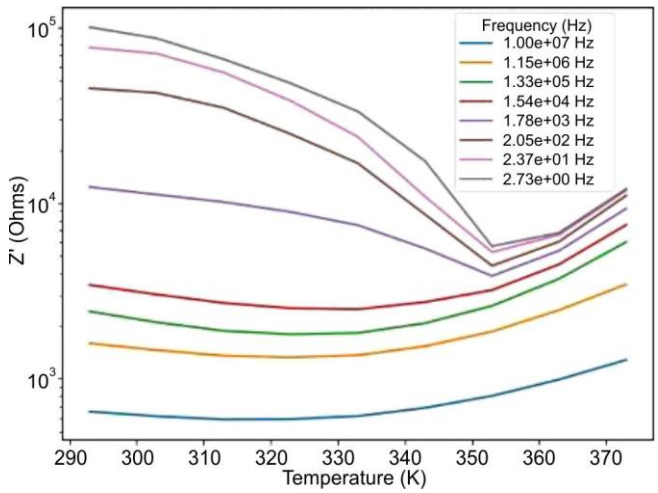

Fig. 5. Plot of Z′ *versus* temperature for MCS/GO at different frequencies

Both temperature- and frequency-dependent impedance trends clearly show that the MCS/GO nanocomposite follows a temperature dependent conduction process, along with strong interfacial and dipolar polarization effects. Such behaviour is typical of polymer-based nanocomposites that respond to both magnetic and electric fields. These properties make MCS/GO a promising material for electronic applications, particularly those that demand stable electrical behaviour and dependable thermal performance over a broad range of operating frequencies.

Frequency-dependent Z″ behaviour of MCS/GO nanocomposite: Broad relaxation peaks at lower temperatures are revealed by the fluctuation of the imaginary part of impedance (Z″) with frequency (Fig. 6), suggesting the existence of temperature-dependent relaxation phenomena controlled by several processes with different relaxation durations [23]. The broadening of these peaks indicates the presence of space-charge effects, likely caused by charge buildup at grain boundaries or defect sites [24]. As the temperature increases, the peak gradually shifts to higher frequencies and its magnitude also shows a decrease. With increase in temperature, charge carriers respond more effectively to the alternating electric field, making the relaxation process faster thereby activating additional relaxation pathways.

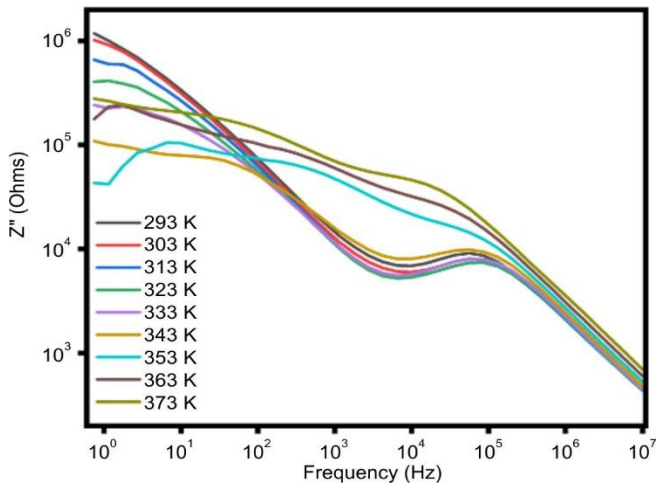

Fig. 6. Plot of Z″ *versus* frequency for MCS/GO at different Temperatures

The imaginary part of the impedance, Z″, reflects the energy which is lost within the material through capacitive and inductive effects. As the temperature rises, at low frequencies, Z″ decreases significantly from an initial high value suggesting better conductivity due to thermally activated motion of charge carriers. However, at high frequencies (around 10^6–10^7 Hz), all Z″ curves merge to nearly the same value regardless of temperature. This behaviour suggests that in this frequency range, fast electronic or dipolar polarization processes dominate the response and are unaffected by the slower movement of ions.

The variation of Z″ with frequency and temperature shows that different relaxation mechanisms are working together. At low frequencies, thermal activation increases the mobility of charge carriers thus improving conductivity. In contrast, at high frequencies, the response remains mostly unaffected by temperature, indicating that these faster polarization processes are temperature independent.

Temperature-dependent Z″ behaviour of MCS/GO nanocomposite: Fig. 7 illustrates the variation of Z″ with temperature across a wide frequency range. A characteristic trend is observed: Z″ decreases with increasing temperature up to ~343 K, after which it begins to rise again. This behaviour, consistent across most frequencies, highlights a transition in the dominant dielectric relaxation mechanism. The increased mobility of thermally activated charge carriers is responsible for the first decline, which reduces polarization lag and energy storage, lowering Z″. The subsequent increase beyond 343 K suggests the onset of additional thermally activated processes, such as interfacial polarization and structural rearrangements within the composite.

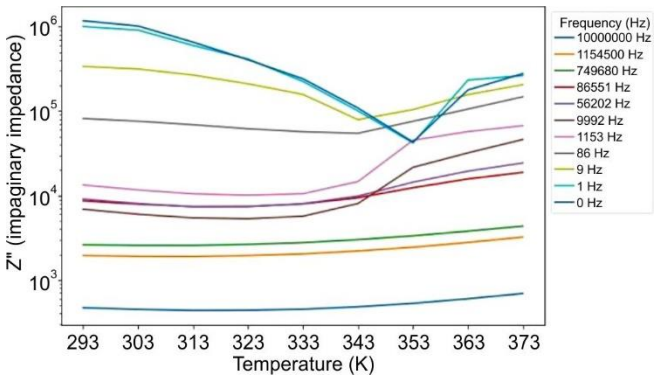

Fig. 7. Plot of Z″ *versus* temperature for MCS/GO at different frequencies

In the low to mid frequency range (≤ 10^4 Hz), the Z″ values form a noticeable V-shaped pattern as the temperature changes. At first, Z″ either decreases slightly or stays almost the same and then it begins to rise gently as the temperature goes above about 345 K. This happens beause an increase in temperature causes charge carriers to gather at the boundaries between MNP/GO or MGO/CS, creating interfacial polarization. At higher frequencies (≥ 10^7 Hz), Z″ becomes large as the charge carriers cannot move fast enough to follow the rapidly changing electric field. As a result, polarization is incomplete and more energy is stored in the material. As the temperature increases, Z″ at high frequencies initially decreases, indicating faster carrier relaxation due to enhanced mobility. It then rises again, likely due to restricted motion of the chitosan chains or structural rearrangements within the composite.

The Z″ behaviour is strongly affected by the materials inside the composites. Graphene oxide (GO), which contains many oxygenated functional groups and surface defects, helps create interfacial and dipolar polarization and also supports easier local charge movement. Chitosan (CS), which has polar -OH and -NH_2 groups, allows small segments of its chain to move and dipoles to reorient, especially near its glass transition temperature. Magnetite (Fe_3O_4) nanoparticles also influence the charges move and the formation of local electric fields, contributing to the overall relaxation effects observed in the material.

The drop in Z″ around 343 K is important as it suggests that a temperature driven relaxation process is taking place. This could be caused by small movements within the chitosan matrix, the activation of dipoles in the material or the beginning of the dominant α-relaxation. When the temperature rises above 343 K, the interfacial polarization (Maxwell–Wagner–Sillars) becomes stronger. As a result, the material stores more energy, which shows up as an increase in Z″ values.

The behaviour of Z″ across different temperatures and frequencies clearly shows that MCS/GO nanocomposite undergoes complex dielectric relaxation. GO improves the interfacial interactions and polarization, while the magnetic nanoparticles help control the material's conductivity and charge storage capacity. Together these effects make the composite suitable for capacitive sensing, energy-storage devices and dielectric components that remain stable even at high temperatures.

Using Z″ to estimate activation energy *via* Arrhenius law: The activation energy (E_a) was calculated using the Arrhenius relation: $\tau_{max} = \tau_0 \exp(E_a/k_bT)$. Here τ_{max} (which is equal to $1/f_{max}$) is the time corresponding to the frequency where the imaginary part of impedance (Z''_{max}) reaches its peak value. In this formula, k_b is the Boltzmann constant and τ_0 is the pre-exponential factor. Fig. 8 presents the plot of $\ln(\tau_{max})$ against 1/T. A linear fit of $\ln(\tau_{max})$ *versus* 1/T yielded an E_a value of approximately 168 meV for the MCS/ GO composite. The calculated activation energy confirms that the relaxation mechanism in the MCS/GO composite is temperature dependent, indicated that the movement of charge carriers or dipole reorientation within the material requires thermal energy to overcome a certain energy barrier. At lower temperatures, the scarcity of thermally activated carriers leads to slower relaxation, whereas higher temperatures facilitate more rapid relaxation due to probably increased carrier mobility. Relaxation occurs more quickly at higher temperatures as the charge carriers gain additional energy, allowing them to move more efficiently through the material.

This behaviour is characteristic of dielectric materials, where increased thermal energy enhances the mobility of dipoles or charge carriers, thereby influencing the electrical response. The activation energy further provides insight into the strength of interaction between the charge carriers and the material. Such information is crucial for assessing the suitability of the material for dielectric, insulating or energy-storage applications.

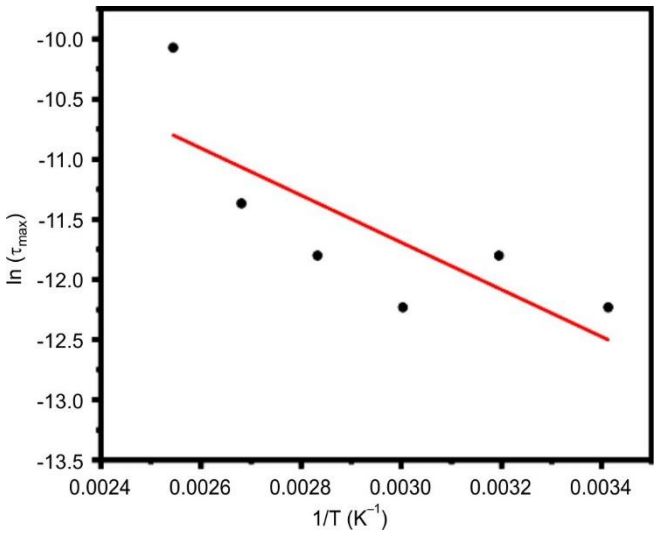

Fig. 8. Arrhenius plot of MCS/GO

The activation energy obtained (~168 meV) matches well with the earlier studies. It is much lower than the values reported for pure chitosen (~320 meV) or Fe_3O_4-CS composites (~240 eV). This lower value indicates that charges can move more easily within the prepared material, primarily since GO contributes to the formation of smoother pathways for carrier hopping. Saravanan [25] report activation energies values for chitosan composites ranging from 36.5 kJ mol^{-1}, for pristine chitosan to ~ 25.7 kJ mol^{-1} for chitosan–graphite–γ-Fe_2O_3. However, literature values for activation energy in chitosan–magnetite and chitosan–GO systems are very limited. Present study addresses this gap by providing activation energy (~168 meV) under temperature and frequency variation. Low activation energy is particularly beneficial for use in solid-state sensors and battery electrodes as it allows charges to movwe more easily and improves charging and discharging performance [26,27].

Electrochemical impedance spectroscopy (EIS) analysis: The Nyquist plots (Fig. 9) depict the variation of impedance with temperature from 293 K to 373 K. As the temperature increases, the overall impedance of the MCS/GO composite decreases, indicating enhanced ionic mobility and improved charge-transfer kinetics at elevated temperatures.

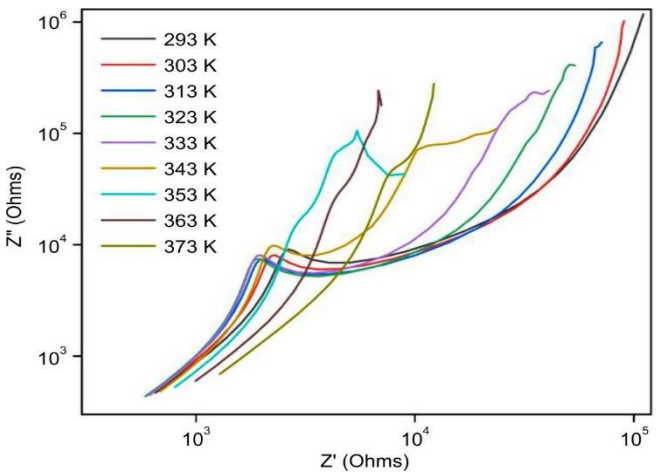

Fig. 9. Nyquist plot (Z′ *vs.* Z″) at different temperatures

High-frequency semicircle (charge-transfer resistance): A distorted/depressed semicircle that represents the charge-transfer resistance (R_{ct}) can be observed in the high-frequency region at all temperatures. The semicircle diameter–proportional to R_{ct}, which decreases markedly from ~10^4 Ω at 293 K to below 10^3 Ω at 373 K, reflecting thermally activated charge-transfer processes [28]. With increasing temperature, the degree of semicircle depression also lessens, indicating reduced surface inhomogeneity and a more uniform distribution of electrochemically active sites.

A key observation is the temperature-dependent shift of the plots toward the origin. At lower temperatures (293-313 K), broader semicircles with larger diameters signify higher R_{ct} and lower conductivity. As the temperature rises (323-373 K), the semicircle diameter progressively decreases, confirming reduced R_{ct} and enhanced charge transport. This overall reduction in impedance with temperature highlights improved ionic conductivity and faster charge-transfer kinetics, validating the thermally activated nature of the mechanism within the MCS/GO nanocomposite.

Mid-frequency and low-frequency features: All Nyquist plots in the low-frequency range show a sloped line that represents Warburg impedance, which results from the diffusion of ions inside the porous electrode structure. As the temperature increases, this line becomes progressively steeper and near 373 K it approaches vertical, indicating a shift toward nearly capacitive behaviour due to accelerated ion diffusion. Apart from the high-frequency charge-transfer semicircle and the low-frequency Warburg tail, subtle shoulder-like features appear in the Nyquist spectra [29,30]. These shoulders become more pronounced in the intermediate temperature range (343-363 K), consistent with thermally activated surface adsorption phenomena. These shoulders disappear at the highest temperature and enters the Warburg diffusion region which implies mass transport controls the behaviour while the capacitive effects at the interface become unimportant. As the temperature increases, both real and imaginary parts of the impedance decrease showing faster movements of ions. The charge-transfer resistance (R_{ct}) also drops exponentially with temperature (Table-1), following normal Arrhenius behaviour, which means that the system allows charges to transfer faster at higher temperatures.

TABLE-1
VALUE OF R_{ct} AT VARIOUS TEMPERATURES

Temperature (K)	Approx. R_{ct} (Ω)
293	220696
303	179574
313	141624
323	100820
333	80572
343	45632
353	9300
363	11696
373	21840

Conclusion

The successful formation of a magnetite-based chitosan/graphene oxide nanocomposite with nanoscale crystalline

Fe_3O_4 uniformly embedded within the matrix. Morphological and elemental analyses show well-distributed particles and strong interfacial contact, while thermal studies revealed significant improved stability due to the reinforcing action of GO. The electrical and dielectric measurements indicate that the composite exhibits temperature- and frequency-dependent conduction governed by interfacial, dipolar and space-charge polarization. A clear shift in relaxation behaviour around 343–353 K, accompanied by reduced Z′ and Z″ values, reflects enhanced charge mobility at elevated temperatures. The activation energy (~168 meV) is significantly lower than in many chitosan-based ferrite systems, suggesting that GO provides favourable pathways for carrier hopping. EIS data further support this, showing a steady decline in charge-transfer resistance and faster ion diffusion with rising temperature. Collectively, the structural integrity, thermal robustness, low energy barrier for charge motion and efficient relaxation dynamics make the MCS/GO composite a strong candidate for dielectric components, sensors and energy-storage applications.

ACKNOWLEDGEMENTS

The authors gratefully acknowledge the University Science Instrumentation Centre (USIC), University of Delhi, for accessing the characterization facilities. Thanks are also due to The Principal, Acharya Narendra Dev College, for providing the infrastructural and institutional support. This work was supported by the DBT STAR College Scheme, Department of Biotechnology, Government of India.

CONFLICT OF INTEREST

The authors declare that there is no conflict of interests regarding the publication of this article.

REFERENCES

1. A. Kausar, *J. Plast. Film Sheeting*, **36**, 94 (2020); https://doi.org/10.1177/8756087919849459
2. P.K. Dutta, J. Duta and V.S. Tripathi, *J. Sci. Ind. Res. (India)*, **63**, 20 (2004).
3. M.A. Salam, *J. Mol. Liq.*, **233**, 197 (2017); https://doi.org/10.1016/j.molliq.2017.03.023
4. A. ZabihiSahebi, S. Koushkbaghi, M. Pishnamazi, A. Askari, R. Khosravi and M. Irani, *Int. J. Biol. Macromol.*, **140**, 1296 (2019); https://doi.org/10.1016/j.ijbiomac.2019.08.214
5. M.A. Ahmed, M.A. Ahmed and A.A. Mohamed, *RSC Adv.*, **13**, 5337 (2023); https://doi.org/10.1039/D2RA07883J
6. E.S. Motiee, S. Karbasi, E. Bidram and M. Sheikholeslam, *Int. J. Biol. Macromol.*, **247**, 125593 (2023); https://doi.org/10.1016/j.ijbiomac.2023.125593
7. L. Shao, X. Chang, Y. Zhang, Y. Huang, Y. Yao and Z. Guo, *Appl. Surf. Sci.*, **280**, 989 (2013); https://doi.org/10.1016/j.apsusc.2013.04.112
8. I.J. Budiarso, N.D. Rini, A. Tsalsabila, M.D. Birowosuto and A. Wibowo, *ACS Biomater. Sci. Eng.*, **9**, 3084 (2023); https://doi.org/10.1021/acsbiomaterials.3c00216
9. M. Verma, S. Rani, K.S. Anugrah, A. Singh, L. Saya and S. Hooda, *J. Mol. Struct.*, **1325**, 141014 (2025); https://doi.org/10.1016/j.molstruc.2024.141014
10. S. Rani, S.K. Ali, P. Kumar, K.S. Anugrah, L. Saya, G. Gambhir, D. Gautam, S. Hooda and M. Verma, *Polimery*, **68**, 386 (2023); https://doi.org/10.14314/polimery.2023.7.4
11. S. Majumdar, P. Sen and R. Ray, *Mater. Res. Bull.*, **151**, 111814 (2022); https://doi.org/10.1016/j.materresbull.2022.111814
12. A.M. Díez-Pascual, *Polymers*, **13**, 2978 (2021); https://doi.org/10.3390/polym13172978
13. F. Ahmad, M. Zahid, H. Jamil, M.A. Khan, S. Atiq, M. Bibi, K. Shahbaz, M. Adnan, M. Danish, F. Rasheed, H. Tahseen, M.J. Shabbir, M. Bilal and A. Samreen, *J. Energy Storage*, **72**, 108731 (2023); https://doi.org/10.1016/j.est.2023.108731
14. V. Khandegar, P.J. Kaur and P. Chanana, *BioResources*, **16**, 8525 (2021); https://doi.org/10.15376/biores.16.4.8525-8566
15. N.I. Zaaba, K.L. Foo, U. Hashim, S.J. Tan, W.W. Liu and C.H. Voon, *Procedia Eng.*, **184**, 469 (2017); https://doi.org/10.1016/j.proeng.2017.04.118
16. L. Saya, W. Rameshwor Singh and S. Hooda, *J. Environ. Chem. Eng.*, **11**, 110766 (2023); https://doi.org/10.1016/j.jece.2023.110766
17. M.F. Latifa, A. Jiananda, A. Riyanto, E.K. Sari, F.S. Sitorus, N.I. Istiqomah and E. Suharyadi, *J. Phys. Conf. Ser.*, **2734**, 012040 (2024); https://doi.org/10.1088/1742-6596/2734/1/012040.
18. J.W. Rhim, S.I. Hong, H.M. Park and P.K. Ng, *J. Agric. Food Chem.*, **54**, 5814 (2006); https://doi.org/10.1021/jf060658h
19. G. Li, Y. Jiang, K. Huang, P. Ding and J. Chen, *J. Alloys Compd.*, **466**, 451 (2008); https://doi.org/10.1016/j.jallcom.2007.11.100
20. J. Suchanicz, *Mater. Sci. Eng. B*, **55**, 114 (1998); https://doi.org/10.1016/S0921-5107(98)00188-3
21. A.R. James and K. Srinivas, *Mater. Res. Bull.*, **34**, 1301 (1999); https://doi.org/10.1016/S0025-5408(99)00127-0
22. M. Samet, V. Levchenko, G. Boiteux, G. Seytre, A. Kallel and A. Serghei, *J. Chem. Phys.*, **142**, 194703 (2015); https://doi.org/10.1063/1.4919877
23. P. Dhak, D. Dhak, M. Das, K. Pramanik and P. Pramanik, *Mater. Sci. Eng. B*, **164**, 165 (2009); https://doi.org/10.1016/j.mseb.2009.09.011
24. F.H. Alshammari, *J. Mater. Res. Technol.*, **20**, 740 (2022); https://doi.org/10.1016/j.jmrt.2022.07.046
25. R.P.R. Saravanan, *Progr. Phys. Appl. Mater.*, **3**, 83 (2023); https://doi.org/10.22075/ppam.2023.31598.1063
26. P. Lu, S. Gong, C. Wang, Z. Yu, Y. Huang, T. Ma, J. Lian, Z. Jiang, L. Chen, H. Li and F. Wu, *ACS Nano*, **18**, 7334 (2024); https://doi.org/10.1021/acsnano.3c07023
27. N. Asthana and K. Pal, in eds.: K. Pal and F. Gomes, Polymerized Hybrid Nanocomposite Implementations of Energy Conversion Cells Device, In: Nanofabrication for Smart Nanosensor Applications Elsevier, Chap. 14, pp. 349-397 (2020).
28. M.A. Zabara, G. Katırcı and B. Ülgüt, *J. Phys. Chem. C*, **126**, 10968 (2022); https://doi.org/10.1021/acs.jpcc.2c02396
29. S.A. Watzele, L. Katzenmeier, J.P. Sabawa, B. Garlyyev and A.S. Bandarenka, *Electrochim. Acta*, **391**, 138969 (2021); https://doi.org/10.1016/j.electacta.2021.138969
30. N. Meddings, M. Heinrich, F. Overney, J.S. Lee, V. Ruiz, S. Seitz, E. Napolitano, G. Hinds, R. Raccichini, M. Gaberšček and J. Park, *J. Power Sources*, **480**, 228742 (2020); https://doi.org/10.1016/j.jpowsour.2020.228742